Turbulence Measurements in the Surf Zone*

JOHN TROWBRIDGE AND STEVE ELGAR

Woods Hole Oceanographic Institution, Woods Hole, Massachusetts

(Manuscript received 14 August 2000, in final form 4 January 2001)

ABSTRACT

Velocity measurements within 1 m of the bottom in approximately 4.5-m water depth on a sand beach provide estimates of turbulent Reynolds shear stress, using a dual-sensor technique that removes contamination by surface waves, and inertial-range estimates of dissipation. When combined with wave measurements along a cross-shore transect and nearby wind measurements, the dataset provides direct estimates of the terms in simplified equations for alongshore momentum and turbulence energetics and permits examination of semiempirical relationships between bottom stress and near-bottom velocity. The records are dominated by three events when the measurement site was in the outer part of the surf zone. Near-bottom turbulent shear stress is well correlated with (squared correlation coefficient $r^2 = 0.63$), but smaller than (regression coefficient $b = 0.51 \pm 0.03$ at 95% confidence), wind stress minus cross-shore gradient of wave-induced radiation stress, indicating that estimates of one or more of these terms are inaccurate or that an additional effect was important in the alongshore momentum balance. Shear production of turbulent kinetic energy is well correlated ($r^2 = 0.81$) and consistent in magnitude ($b = 1.1 \pm 0.1$) with dissipation, and both are two orders of magnitude smaller than the depth-averaged rate at which the shoaling wave field lost energy to breaking, indicating that breaking-induced turbulence did not penetrate to the measurement depth. Log-profile estimates of stress are well correlated with ($r^2 = 0.75$), but larger than ($b = 2.3 \pm 0.1$), covariance estimates of stress, indicating a departure from the Prandtl–von Kármán velocity profile. The bottom drag coefficient was $(1.9 \pm 0.2) \times 10^{-3}$ during unbroken waves and approximately half as large during breaking waves.

1. Introduction

Turbulence is believed to have a dominant effect on flows and sediment transport in the surf zone. For example, often it is assumed that a balance between bottom stress and cross-shore gradient of wave-induced radiation stress controls the alongshore flow driven by breaking waves (e.g., Battjes 1988) and that the effect of bottom stress is transmitted through the water column by turbulence with scales much smaller than the water depth (e.g., Svendsen and Putrevu 1994). Breaking-induced turbulence dominates wave energy dissipation in the surf zone (Thornton and Guza 1986). Many models of sediment transport are based on the assumptions that near-bottom turbulent shear stress controls the entrainment of sediment from the seafloor (e.g., Glenn and Grant 1987) and that turbulence maintains suspended sediment in the water column (e.g., Fredsoe and Deigaard 1992; Nielsen 1992).

Despite the importance of turbulence in conceptual and mathematical models of surf zone processes, direct measurements of surf zone turbulence have been rare. Separation of turbulence from waves is difficult because turbulent velocity fluctuations typically are two to three orders of magnitude less energetic than wave motions. As a result, previous surf zone turbulence measurements have focused on velocity fluctuations at frequencies far higher than those of the waves, resulting in estimates of dissipation, but not stress (George et al. 1994), or they have have been obtained in laboratory basins (e.g., Ogston et al. 1995; Ting and Kirby 1996), where phase-averaging techniques appropriate for monochromatic waves, which are not applicable in random ocean waves, are used to separate waves from turbulence. Most estimates of nearshore turbulence statistics have been obtained indirectly from measurements of waves and winds. For example, depth-integrated dissipation has been estimated as the residual in a wave energy balance (Thornton and Guza 1986; Kaihatu and Kirby 1995; Elgar et al. 1997; Herbers et al. 2000), and bottom stress has been estimated as the residual in an alongshore momentum balance (Thornton and Guza 1986; Whitford and Thornton 1996; Feddersen et al. 1998; Lentz et al. 1999).

Here, surf zone measurements of near-bottom velocity designed to produce direct covariance estimates of turbulent Reynolds shear stress and inertial-range esti-

* Woods Hole Oceanographic Institution Contribution Number 10275.

Corresponding author address: Dr. John H. Trowbridge, WHOI, Woods Hole, MA 02543.
E-mail: jtrowbridge@whoi.edu

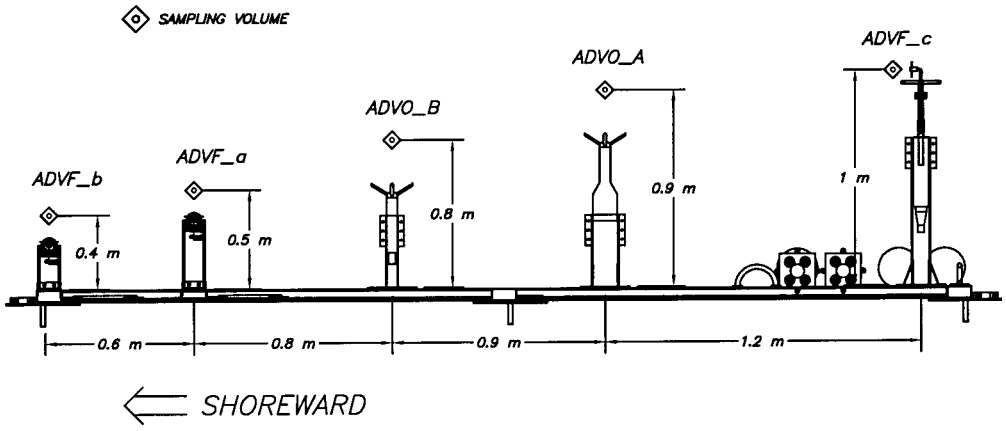

FIG. 1. Array of near-bottom acoustic Doppler current meters deployed in about 4.5-m water depth approximately 300 m from the shoreline. ADVF and ADVO are SonTek field and ocean probes, respectively.

mates of turbulence dissipation are presented. The turbulence measurements were obtained within a cross-shelf transect of arrays of pressure sensors, which determine the wave field, and near an anemometer and a profiling velocimeter, which determine wind forcing and vertical structure of currents. The analysis focuses on estimation of terms in four equations that are commonly used to describe surf zone processes. The first is an alongshore momentum equation, in which wind stress and cross-shore gradient of wave-induced radiation stress balance near-bottom turbulent Reynolds shear stress (e.g., Mei 1983):

$$\tau_{wy} - \frac{dS_{xy}}{dx} = -\rho_0 \overline{v'w'}. \quad (1)$$

The second is a hybrid of a balance between dissipation

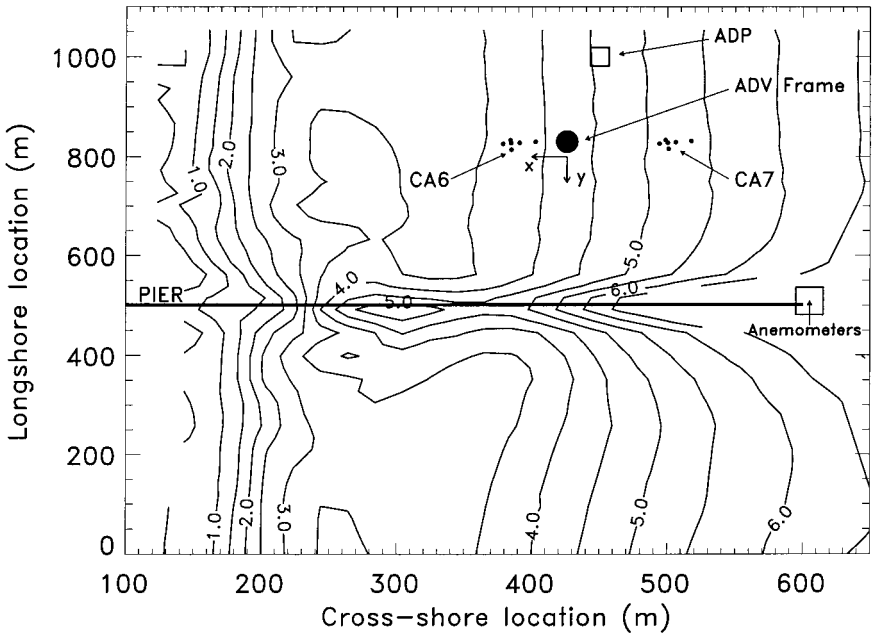

FIG. 2. Locations of instruments (labeled) and contours of water depth (in m below mean sea level every 0.5 m) for yearday 226. Each compact array (CA6 and CA7) contained six accurately ($\pm$0.5 m) surveyed bottom-mounted pressure sensors (small filled circles) and one current meter located about 0.5 m above the bottom near the center of the array (not shown) (Herbers et al. 2000, submitted to *J. Phys. Oceanogr.*). The shoreline location was centered approximately at cross-shore location = 125 m, with $\simeq \pm 10$ m cross-shore fluctuations caused by the 1-m tidal range. The bathymetry seaward of about 3.5-m depth did not change significantly during the experiment.

and shear production of turbulent kinetic energy, known to hold in the wall region of turbulent boundary layers (e.g., Tennekes and Lumley 1972), and a simplified model of surf zone energetics (Battjes 1975), in which dissipation balances the depth-averaged rate at which breaking extracts energy from the shoaling wave field:

$$\epsilon = -\overline{v'w'}\frac{\partial \overline{v}}{\partial z} - \frac{1}{\rho_0(h + \overline{\eta})}\frac{dF_x}{dx}. \quad (2)$$

The third is the Prandtl–von Kármán representation of the velocity profile in a turbulent boundary layer (e.g., Tennekes and Lumley 1972):

$$\rho_0\kappa^2(z + h)^2\left[\left(\frac{\partial \overline{u}}{\partial z}\right)^2 + \left(\frac{\partial \overline{v}}{\partial z}\right)^2\right]^{1/2}\frac{\partial \overline{v}}{\partial z} = -\rho_0\overline{v'w'}, \quad (3)$$

which has been used in the surf zone to estimate stress from measurements of horizontal velocity (Garcez-Faria et al. 1998). The fourth is a quadratic drag law:

$$c_d\rho_0\overline{(u^2 + v^2)^{1/2}v} = -\rho_0\overline{v'w'}, \quad (4)$$

commonly used to represent bottom stress in models of nearshore processes (e.g., Bowen 1969; Longuet-Higgins 1970).

In (1)–(4), x, y, and z are coordinates in a right-handed system with x positive onshore, y positive alongshore, and z positive upward, where $z = -h$ and $z = \eta$ represent the seafloor and water surface, respectively. The quantity ρ_0 is a fixed reference density, (u, v, w) is the velocity vector, primes denote turbulent fluctuations, $-\rho_0\overline{v'w'}$ is the alongshore component of the turbulent Reynolds shear stress, ϵ is the turbulence dissipation rate, F_x is the cross-shore component of the wave-induced energy flux, S_{xy} is the off-diagonal component of the wave-induced radiation stress tensor, τ_{wy} is the alongshore component of the wind stress, κ is the empirical von Kármán constant (approximately equal to 0.40), and c_d is an empirical drag coefficient. An overbar represents a time average over a period long compared with the timescales of waves and turbulence, but short relative to the timescales of variability of the forcing. The wind stress, energy flux, radiation stress, and dissipation are averaged over the same time period. The statistical properties of the flow are assumed to be stationary over the averaging period and independent of alongshore position. The quantity $-\rho_0\overline{v'w'}$ is evaluated at a height above bottom that is small compared with the water depth, but large relative to the scale of the bottom roughness elements, so that it represents the stress transmitted to the seafloor. The stress-transmitting turbulence is assumed to be distinguishable from other motions because of its small spatial scales, believed to be a small fraction of the water depth (e.g., Svendsen and Putrevu 1994).

2. Methods

a. Measurements

The turbulence measurements, described in detail by Fredericks et al. (2001), were acquired between 25 August (yearday 236) and 21 November (yearday 324) of 1997 on a sandy Atlantic beach near Duck, North Carolina, at the U.S. Army Corps of Engineers Field Research Facility. An array of five upward-looking Sontek acoustic Doppler velocimeters (ADVs) was mounted on a low-profile frame (Fig. 1). The ADVs measure the three-dimensional velocity vector in a sample volume with a spatial scale of approximately 0.01 m (e.g., Voulgaris and Trowbridge 1998) and perform well in the surf zone (Elgar et al. 2001). The array included three of the field version of Sontek's acoustic Doppler velocimeter (ADVF) and two of the more rugged ocean version (ADVO), one of which was fitted with pressure, temperature, pitch, and roll sensors, as well as compass. The ADVOs shared a common logger that sampled the two sensors simultaneously at 7 Hz in one burst of 25 minutes each hour. The ADVFs shared a separate common logger that sampled the three sensors simultaneously at 25 Hz in one burst of 10 minutes each hour. The ADV frame was approximately 300 m from the shoreline and 300 m north of the Field Research Facility (FRF: Fig. 2). The ADVs occupied an on–offshore line along the frame's northern edge, upstream of the frame itself, relative to the predominantly southerly wind- and wave-driven flows. The bathymetry near the measurement site is approximately uniform in the alongshore direction on scales of kilometers (Birkemeier et al. 1985; Lentz et al. 1999), although there is a cross-shore channel approximately 100 m wide and 1 m deep beneath the pier (Fig. 2).

Other instrumentation included 12 Setra pressure sensors making up ''compact arrays'' 6 and 7 (CA6 and CA7), centered approximately 40 m onshore and 80 m offshore of the ADV frame, respectively (Herbers et al. 2000, submitted to *J. Phys. Oceanogr.*) two Marsh–McBirney two-axis electromagnetic current meters, located near the centers of CA6 and CA7; a Solent sonic anemometer, located on a mast at the end of the FRF pier approximately 20 m above the water surface; and a Sontek 3-MHz acoustic Doppler profiler (ADP), located approximately 170 m north of the ADV frame (Fig. 2). The pressure sensors and two-axis velocimeters were sampled nearly continuously at 2 Hz, the sonic anemometer was sampled continuously at 21 Hz, and the ADP sampled continuously in 0.25-m range bins at 25 Hz.

The ADV array experienced several problems. Estimates of wave angles indicate that the head of the offshore ADVF began rotating intermittently immediately after deployment. Approximately six days after deployment, the offshore ADVO began malfunctioning, and intermittently produced invalid data, characterized by intervals with velocities of precisely zero or poor correlation with velocities measured by the other ADVO. The ADVO measurements of acoustical backscatter intensity are clipped (i.e., do not exceed a fixed maximum value) during strong flows, which precludes use of this measurement to infer sediment concentration. Approx-

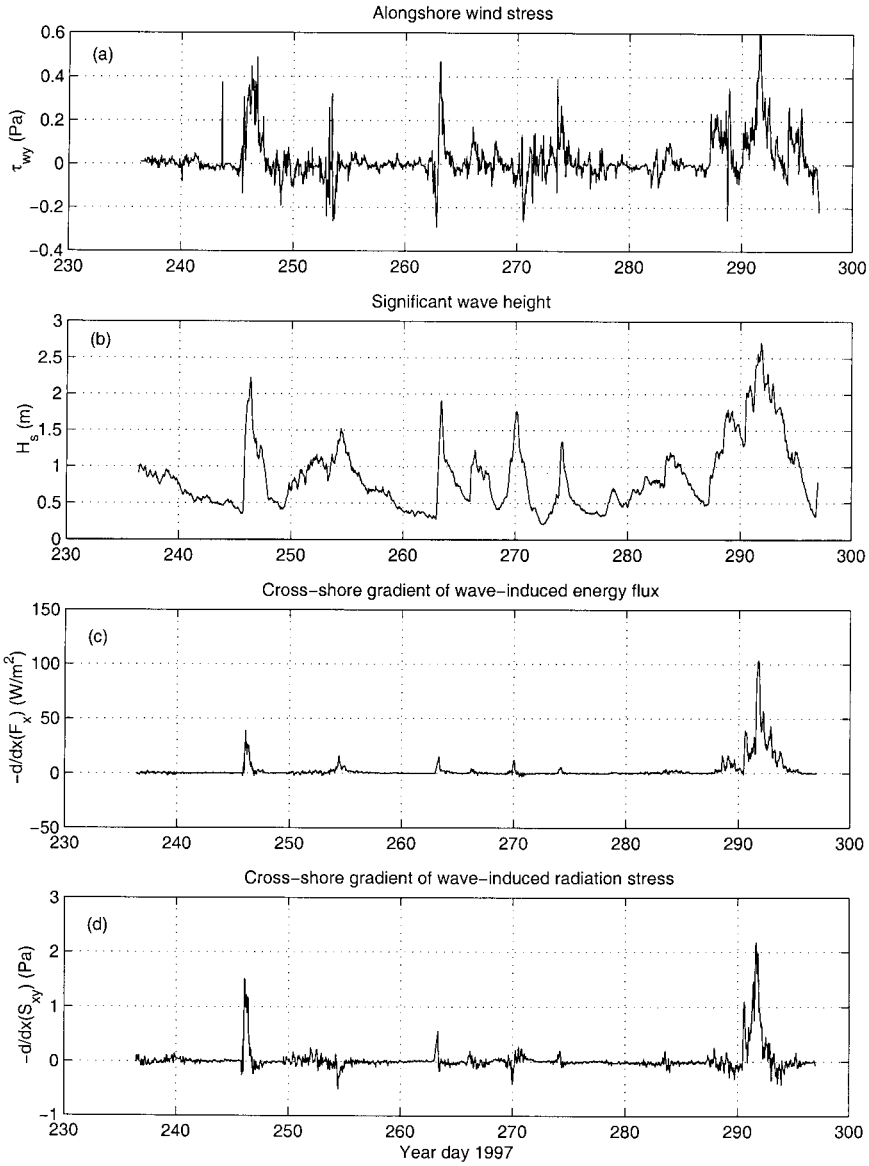

FIG. 3. (a) Alongshore wind stress, (b) significant wave height, (c) cross-shore gradient of wave-induced energy flux, and (d) cross-shore gradient of wave-induced radiation stress vs time.

imately ten days after deployment, the two onshore ADVFs were destroyed by large waves and strong currents. Divers reported that a scour hole with a depth of roughly 0.2 m formed beneath the ADV frame within a few days of deployment and that sand worms colonized the frame during the final two weeks, terminating useful data on approximately 27 October (yearday 299).

b. Analysis

The analysis focuses on data produced by the ADVOs and the two onshore ADVFs during the first six days of the measurement period, when these four sensors functioned well, and on the remainder of the records produced by the ADVOs during intervals when the offshore ADVO produced valid data. To identify valid segments in the record produced by the offshore ADVO [see Fredericks et al. (2001) for details], the ADVO records were divided into 100-sample blocks, and the squared correlation coefficient r^2 between cross-shore velocities at the two ADVOs was calculated for each block. Data from the intermittently functioning ADVO were assumed valid for blocks with $r^2 > 0.90$. Thresholds of $r^2 = 0.90$ and $r^2 = 0.80$ produced nearly identical results.

Separate estimates of the alongshore component of turbulent Reynolds shear stress were obtained from the pair of ADVOs and from the onshore pair of ADVFs,

by means of the dual-sensor procedure described by Trowbridge (1998):

$$-\rho_0\overline{v'w'} = -(1/2)\rho_0 \operatorname{cov}(\Delta v, \Delta w), \qquad (5)$$

where Δv and Δw are differences between alongshore and vertical velocities measured at two sensors, and cov is covariance. Equation (5) is based on the assumption that the stress-carrying turbulence has scales much smaller than scales of other motions, including in particular surface waves, and it requires that the sensor separation be such that the wave-induced velocities at the two sensors are nearly identical, while the corresponding turbulent velocities are uncorrelated. In addition to sampling variability, stress estimates based on (5) have a wave bias, caused by imperfect cancellation of wave-induced velocities by the differencing operation, and a turbulence bias, caused by nonzero correlation between turbulent velocity fluctuations at the two sensors. Estimates based on the analysis of Trowbridge (1998) indicate that the wave bias in the alongshore stress is an order of magnitude smaller than the alongshore stress itself in the present case. In contrast, wave biases in estimates of the cross-shore stress are similar in magnitude to the cross-shore stress so that the measurements provide only order-of-magnitude estimates of the cross-shore stress. The turbulence bias is discussed in section 4.

Estimates of dissipation were obtained from the onshore ADVO data by applying an inertial-range turbulence model to velocity spectra. The model, which describes frozen inertial-range turbulence advected past a fixed sensor by a steady horizontal current and random waves (Lumley and Terray 1983), was specialized (see the appendix) for frequencies large compared with the dominant wave frequency, unidirectional waves, and conditions near the seafloor, where wave-induced vertical velocities have a negligible effect on advection of turbulence. The model representation of the sum of the spectra of the two horizontal components of velocity is

$$P_{uu}(\omega) + P_{vv}(\omega) = \frac{21}{55}\alpha\epsilon^{2/3}V^{2/3}\omega^{-5/3}I\left(\frac{\sigma}{V}, \theta\right) + \text{constant noise level}, \qquad (6)$$

and the model representation of the spectrum of vertical velocity is

$$P_{ww}(\omega) = \frac{12}{55}\alpha\epsilon^{2/3}V^{2/3}\omega^{-5/3}I\left(\frac{\sigma}{V}, \theta\right), \qquad (7)$$

where P_{uu}, etc., are spectra, defined so that $\int_{-\infty}^{+\infty} P_{uu}(\omega)\, d\omega$ = variance; ω is radian frequency, equal to $2\pi f$, where f is cyclic frequency; α is the empirical Kolmogorov constant, approximately equal to 1.5 (Grant et al. 1962); V is the magnitude of the current; σ^2 is the variance of the wave-induced horizontal velocity; θ is the angle between waves and current; and $I(\sigma/V, \theta)$ is defined in the appendix. For each burst from the onshore ADVO, V, σ, and θ were set equal to the magnitude of the mean horizontal velocity, the standard deviation of the horizontal velocity, and the angle between the principal axes of the horizontal velocity fluctuations and the direction of the mean velocity, respectively. Burst-averaged velocity spectra P_{uu}, etc., were obtained by combining spectra from Hanning windowed 100-sample segments. The noise level in (6) was estimated as the average of $P_{uu} + P_{vv}$ over cyclic frequencies greater than 3 Hz. Two independent estimates of burst-averaged dissipation were obtained by averaging estimates of $\omega^{5/3}$ [$P_{uu}(\omega) + P_{vv}(\omega)$ − noise level] and $\omega^{5/3}P_{ww}(\omega)$ over cyclic frequencies between 1 and 2 Hz, and solving (6) and (7) for ϵ. The two estimates are well correlated ($r^2 = 0.95$) and approximately consistent in magnitude (regression slope $b = 0.78 \pm 0.1$ at 95% confidence). The two estimates were then averaged to produce a single estimate of dissipation.

The estimates of dissipation are based on several considerations. Measured spectra are consistent with the model assumptions that P_{ww} is noise-free and that $P_{uu} + P_{vv}$ has a constant noise level (section 3; see also Elgar et al. 2001). The model fit is restricted to frequencies between 1 and 2 Hz because the measurements indicate applicability of (6) and (7) in this range (section 3) and because estimates of the spatial scales of turbulence corresponding to this range of frequencies, combined with atmospheric velocity spectra (Kaimal et al. 1968), indicate applicability of the inertial-range model. Equations (6) and (7) were not applied to ADVF data because, in contrast to the ADVO data, $\omega^{5/3}$ times spectral density minus noise for ADVF measurements was not constant at high frequency, instead exhibiting one or more peaks suggesting input of energy by flow disturbances produced by sensor supports and electronics, which were not far below the ADVF sample volumes (Fig. 1). High-frequency noise problems similarly precluded use of (6) and (7) with the offshore ADVO data.

Hour-averaged estimates of sea surface elevation variance, energy flux, and radiation stress in the wind wave frequency band ($0.04 < f < 0.31$ Hz) were obtained from the arrays of bottom-mounted pressure sensors using linear wave theory and a directional-moment-estimation technique (Elgar et al. 1994; Herbers et al. 1995; Herbers et al. 1999). Estimates obtained from the pressure arrays are well correlated and consistent in magnitude with independent estimates using linear theory from collocated measurements of pressure and velocity.

Records of F_x and S_{xy} at CA6 and CA7 were differenced to determine dF_x/dx and dS_{xy}/dx. Estimates of dS_{xy}/dx are sensitive to errors in orientation, so a simplified procedure was used to estimate and correct for misalignment. The compact arrays CA6 and CA7 were assumed to be in coordinate systems rotated about the z axis by small angles $\gamma^{(6)}$ and $\gamma^{(7)}$ with respect to the isobath-aligned coordinate system. The radiation stress

S_{xy} at compact array n in isobath-aligned coordinates is then (e.g., Jeffreys 1974)

$$S_{xy}^{(n)} = \hat{S}_{xy}^{(n)} + \gamma^{(n)}[\hat{S}_{xx}^{(n)} - \hat{S}_{yy}^{(n)}] + O(\gamma^2), \quad (8)$$

where $\hat{S}_{xx}^{(n)}$, etc., are components of the radiation stress tensor at array n in the slightly misaligned coordinate system. It follows from (8) that

$$\Delta S_{xy} = \Delta\hat{S}_{xy} + (\hat{S}_{xx} - \hat{S}_{yy})_{\text{avg}}\Delta\gamma + \Delta(\hat{S}_{xx} - \hat{S}_{yy})\gamma_{\text{avg}} + O(\gamma^2), \quad (9)$$

where Δ and subscript avg denote the difference and the average, respectively, of the values at CA6 and CA7. With the assumption that the misalignments are of similar magnitude but unequal (i.e., $\Delta\gamma$ is order γ_{avg}), while differences between radiation stresses at CA6 and CA7 are small compared with the radiation stresses themselves (i.e., $\Delta[\hat{S}_{xx} - \hat{S}_{yy}] \ll [\hat{S}_{xx} - \hat{S}_{yy}]_{\text{avg}}$), (9) approximates

$$\Delta S_{xy} = \Delta\hat{S}_{xy} + (\hat{S}_{xx} - \hat{S}_{yy})_{\text{avg}}\Delta\gamma. \quad (10)$$

To estimate $\Delta\gamma$, ΔS_{xy} was assumed equal to zero when the significant wave height H_s (four times the standard deviation of sea surface displacement) at CA7 was less than 1 m, corresponding to nonbreaking waves. For these conditions, $\Delta\hat{S}_{xy}$ was regressed against $-(\hat{S}_{xx} - \hat{S}_{yy})_{\text{avg}}$, yielding $\Delta\gamma = 3.1 \pm 0.1$ degrees at 95% confidence. Equation (10) with this value of $\Delta\gamma$ was then used to compute ΔS_{xy} at all times, including those when $H_s > 1$ m at CA7.

Hour-averaged estimates of τ_{wy} were determined from covariances of horizontal and vertical velocities computed from demeaned and detrended 10-min records from the sonic anemometer. These estimates are well correlated ($r^2 = 0.85$) and consistent in magnitude ($b = 1.35 \pm 0.04$) with independent estimates from a nearby mechanical anemometer (Fredericks et al. 2001).

Estimates of $\partial\overline{u}/\partial z$ and $\partial\overline{v}/\partial z$ at approximately the measurement height of the ADVOs were obtained by differencing hour-averaged velocities in ADP bins 1 and 3, 0.63 and 1.13 m above the seafloor, respectively. The ADP data begin at yearday 262, so there are no estimates of velocity gradient for the first 26 days of the ADV record.

3. Results

During most of the measurement period, winds were weak, waves were small, and the 4.5-m-depth ADV site was seaward of the surf zone. During a few events, however, the alongshore wind stress approached 0.5 Pa (Fig. 3a), the significant wave height reached or exceeded 2 m (Fig. 3b), and shoreward-propagating waves lost energy flux (Fig. 3c) and produced a cross-shore gradient of wave-induced radiation stress (Fig. 3d), presumably because of breaking. The strong winds and breaking waves forced strong alongshore currents (Fig. 4b), in some cases accompanied by strong cross-shore currents (Fig. 4a), particularly during three events centered on days 246, 263, and 292. During these events, $\overline{v}$ and $\partial\overline{v}/\partial x$ had the same sign (Figs. 4b and 4c), suggesting that the ADV site was in the outer part of the surf zone, because the strength of the alongshore current increased with increasing distance onshore. The fraction of valid data from the malfunctioning ADVO was high during the three strong flow events (Fig. 4d).

Velocity spectra indicate energetic wave motions at cyclic frequencies f between approximately 0.05 and 0.5 Hz (Fig. 5a). At higher frequencies, spectra of horizontal and vertical velocity are consistent with isotropic inertial-range turbulence, as described by (6) and (7), because $f^{5/3}P_{ww}$ and $(12/21)f^{5/3}(P_{uu} + P_{vv} -$ noise level) are nearly independent of f and nearly equal to each other (Fig. 5b). Cospectra of differences between alongshore and vertical velocities measured by the two ADVOs (Fig. 5c), which illustrate the frequency content of dual-sensor estimates of turbulent Reynolds shear stress based on (5), indicate significant contributions to stress between approximately 0.01 and 1.0 Hz. The spectra and cospectra in Fig. 5 are representative of the first six days of the record, when four ADVs functioned well, waves were unbroken, and flows were weak. Spectral shapes for periods with breaking waves are similar. Cospectra of Δv and Δw during breaking waves were not computed because of short records caused by intermittent malfunctioning of the offshore ADVO (section 2).

Measurements from the beginning of the record, when both ADVOs and the onshore pair of ADVFs functioned well, permit a comparison of redundant stress estimates. The four single-sensor estimates $-\rho_0\overline{v'w'} = -\rho_0\,\text{cov}(v, w)$ from individual ADVs (Fig. 6a) are contaminated by waves, and thus are uncorrelated with each other and vary over a range much larger than the wind and wave forcing during this period (Figs. 3a and 3d). In contrast, stress estimates from the pair of ADVFs and the pair of ADVOs (Fig. 6b) are well correlated ($r^2 = 0.62$), consistent in magnitude ($b = 1.0 \pm 0.2$ at 95% confidence), and much smaller than the single-sensor estimates.

Time series of the terms in (1)–(4) are dominated by a few brief events when strong winds and waves forced energetic flows. Estimates of the left and right sides of (1) (Figs. 7a and 7b) are well correlated ($r^2 = 0.63$), but the turbulent Reynolds stress is approximately half the sum of the wave and wind forcing ($b = 0.51 \pm 0.03$). In (2), dissipation and shear production are well correlated ($r^2 = 0.70$) and consistent in magnitude ($b = 1.1 \pm 0.1$), even though dissipation was large while shear production was small during an event centered on day 270 (Figs. 8a and 8b). Dissipation and shear production are two orders of magnitude smaller than the depth-averaged rate at which the shoaling waves lose energy to breaking (Fig. 8c). Estimates of $-\rho_0\overline{u'w'}$ obtained from an expression analogous to (5) indicate that the production term $-\overline{u'w'}\,\partial\overline{u}/\partial z$, which has been neglected in (2), is an order of magnitude smaller than

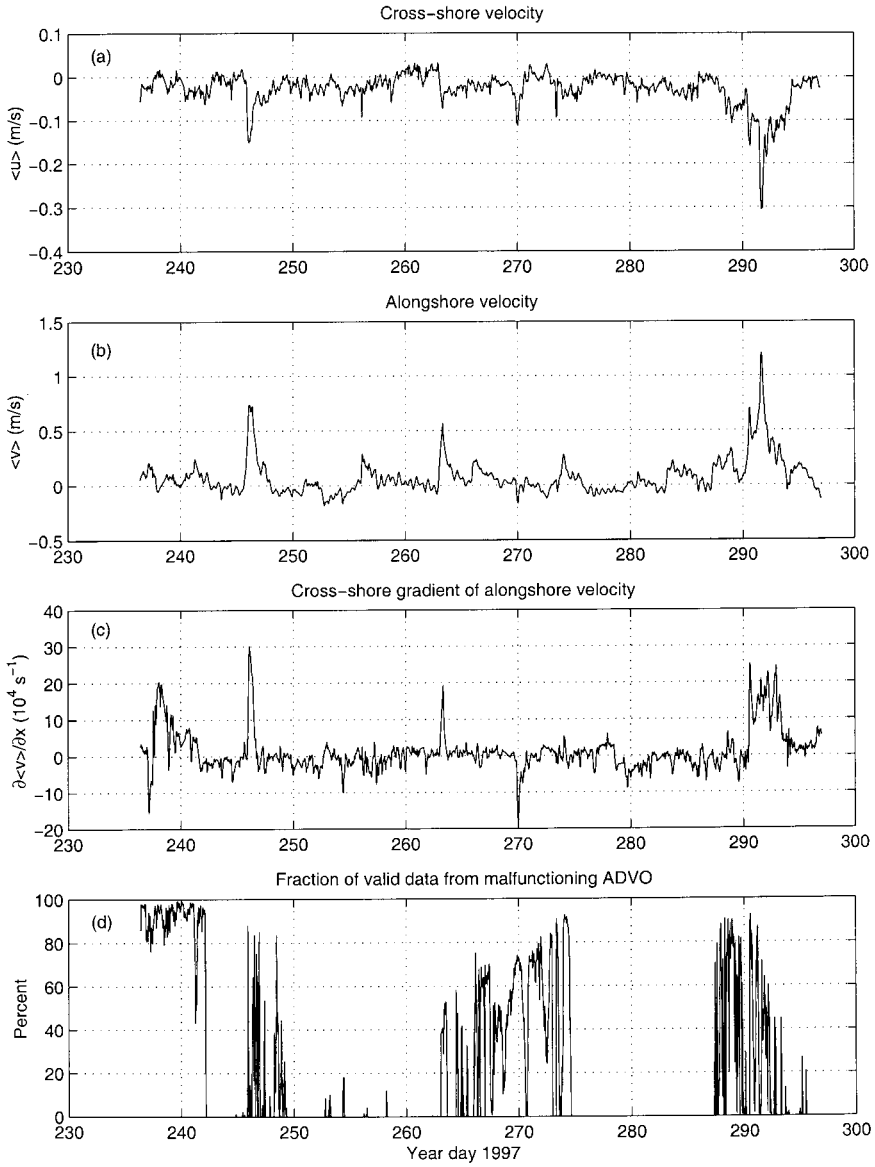

FIG. 4. (a) Cross-shore velocity (negative is offshore-directed flow), (b) alongshore velocity (positive is flow toward the south), (c) cross-shore gradient of alongshore velocity, and (d) percent of valid data from the malfunctioning ADVO vs time.

$-\overline{v'w'}\,\partial\overline{v}/\partial z$. Estimates of the terms on the right and left sides of (3) (Figs. 9a and 9b) are well correlated ($r^2 = 0.75$), but log-profile estimates of alongshore stress are approximately twice as large as estimates based on (5) ($b = 2.2 \pm 0.1$), indicating a departure from the Prandtl–von Kármán logarithmic velocity profile. A quadratic drag law with a best-fit drag coefficient of $c_d = (0.71 \pm 0.03) \times 10^{-3}$ (Figs. 9a and 9c) is well correlated with stress estimates based on (5) ($r^2 = 0.80$). Corresponding estimates during periods with unbroken waves and weak flows ($\overline{v} < 0.2$ m s^{-1}) are weakly correlated ($r^2 = 0.39$) and indicate a larger drag coefficient of $c_d = (1.9 \pm 0.2) \times 10^{-3}$.

Acoustical measurements of bedform geometry on the same isobath as the ADV frame (Hanes and Alymov 2000, submitted to *J. Geophys. Res.*) indicate short ripples, with heights up to 0.02 m and lengths up to 0.25 m, and long ripples, with heights up to 0.06 m and lengths up to 2 m. The heights and inverse wavenumbers of these bedforms are smaller than the ADV measurement heights, indicating that local flow distortions by bedforms had a negligible effect on the ADV measurements.

The results in Figs. 7–9 did not depend sensitively on the rate at which the malfunctioning ADVO produced valid data (Fig. 4d), because the correlation coefficients and regression slopes are not systematic functions of percent of valid data collected.

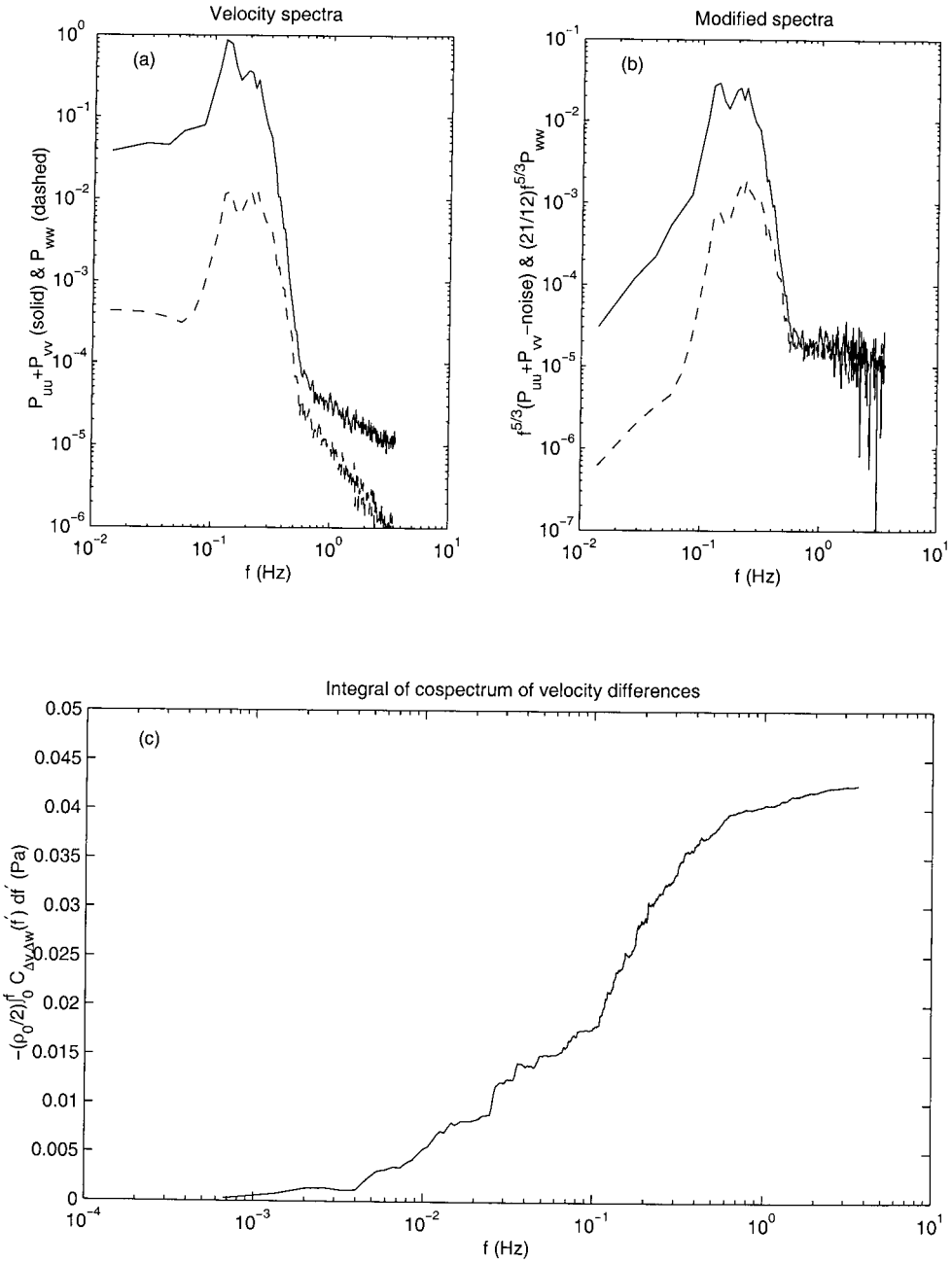

FIG. 5. Energy density spectra from (a) velocity time series and (b) modified according to (6) and (7). Solid curves are $P_{uu} + P_{vv}$ and dashed curves are P_{ww}. (c) Integral of cospectrum of velocity differences vs frequency. Data are from 25-min-long ADVO records obtained at 12:00 (EST) on yearday 236. The burst-averaged cross-shore and alongshore currents were −0.02 and 0.10 m s^{-1}, respectively, and the significant wave height was 1.0 m.

4. Discussion

a. Momentum balance

The factor of 2 difference between the left and right sides of the momentum balance (1) (Fig. 7) might be caused by inaccurate estimates of dS_{xy}/dx or $-\rho_0 \overline{u'\omega'}$. Inaccurate estimation of τ_{wy} is unlikely to be responsible because τ_{wy} was not a dominant term (compare Fig. 3a with Fig. 3d) and because of the consistency of wind stress estimates from sonic and mechanical anemometers (section 2). Inaccurate estimates of dS_{xy}/dx might result from use of linear wave theory to relate bottom pressure to S_{xy} or from the approximate procedure used to resolve uncertainties in sensor orientation (section 2). Estimates of $-\rho_0 \overline{u'w'}$ based on (5) are too small, possibly explaining the observed differences between the

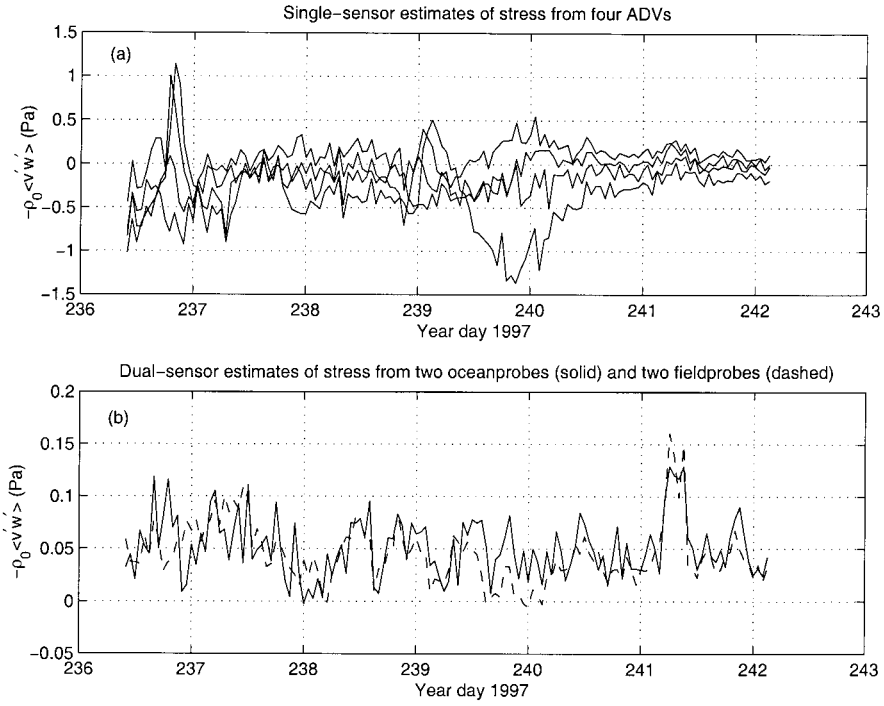

FIG. 6. Estimates of near-bottom stress using (a) single and (b) dual sensors vs time. (b) Estimates from the pair of ADVOs and ADVFs are shown as solid and dashed curves, respectively.

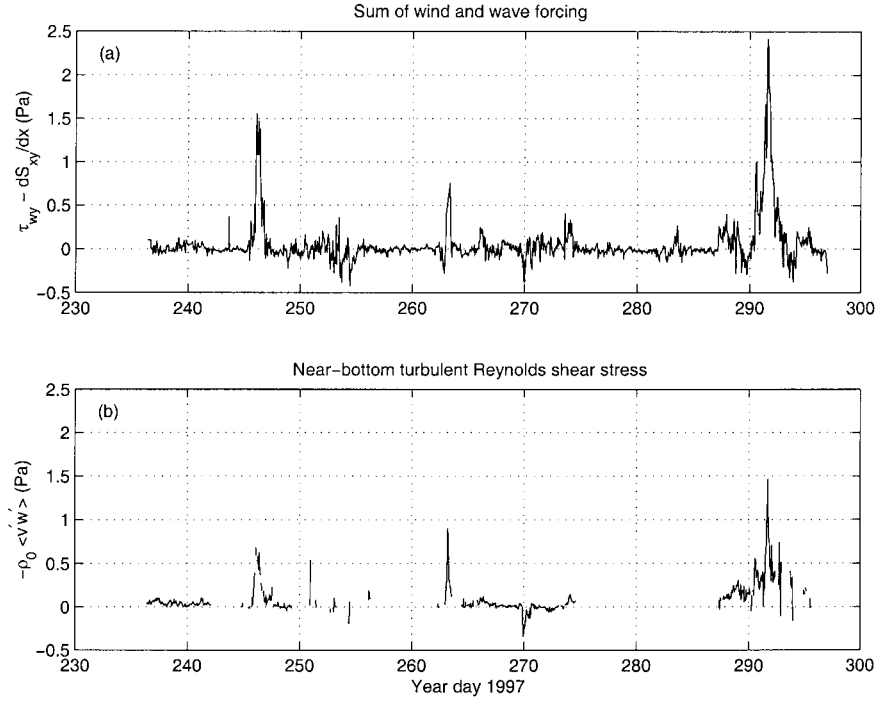

FIG. 7. (a) Sum of wind and wave forcing and (b) near-bottom turbulent Reynolds shear stress vs time.

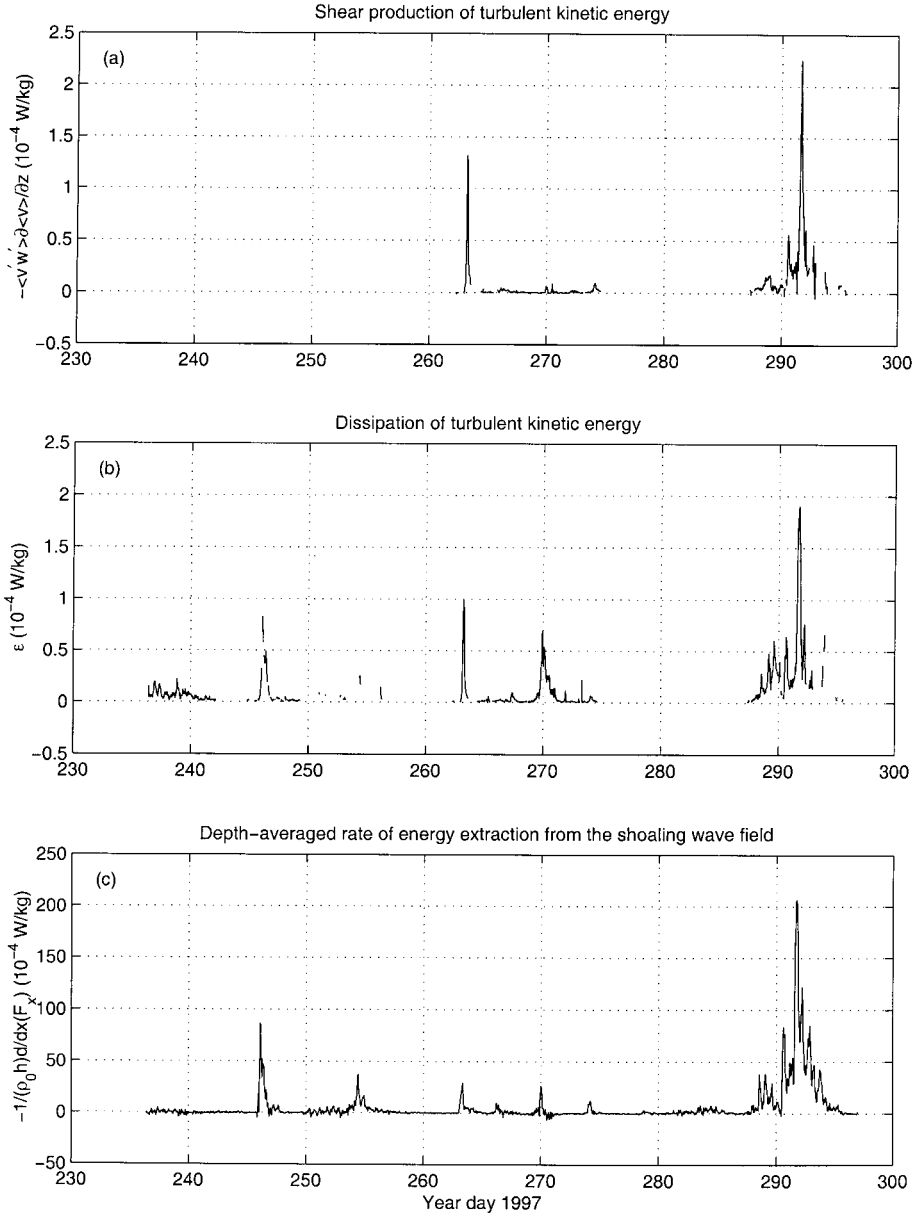

FIG. 8. (a) Shear production of turbulent kinetic energy, (b) dissipation of turbulent kinetic energy, and (c) depth-averaged rate of energy extraction from the shoaling wave field vs time. The vertical scale in (c) is different than in (a) and (b).

left and right sides of (1) if the distance between the two ADVOs was smaller than the correlation scale of the turbulence. To assess this effect, stress estimates based on (5) were computed using all pairs from the four ADVs that functioned during the first-six days of the record, providing spatial separations ranging from 0.6 to 2.3 m. No significant increase in magnitude of stress estimates occurs with increasing sensor separation during this period. However, turbulence correlation scales might have increased during the more energetic events that dominate Fig. 7, because of advection of turbulence by large wave-induced velocities.

The differences between the left and right sides of (1) might also be caused by omitted terms in the alongshore momentum balance, including divergence of a shoreward flux of alongshore momentum by shear waves (Oltman-Shay et al. 1989; Bowen and Holman 1989), an alongshore pressure gradient, or advective acceleration of the hour-averaged flow. Velocity fluctuations at frequencies below the wind wave band con-

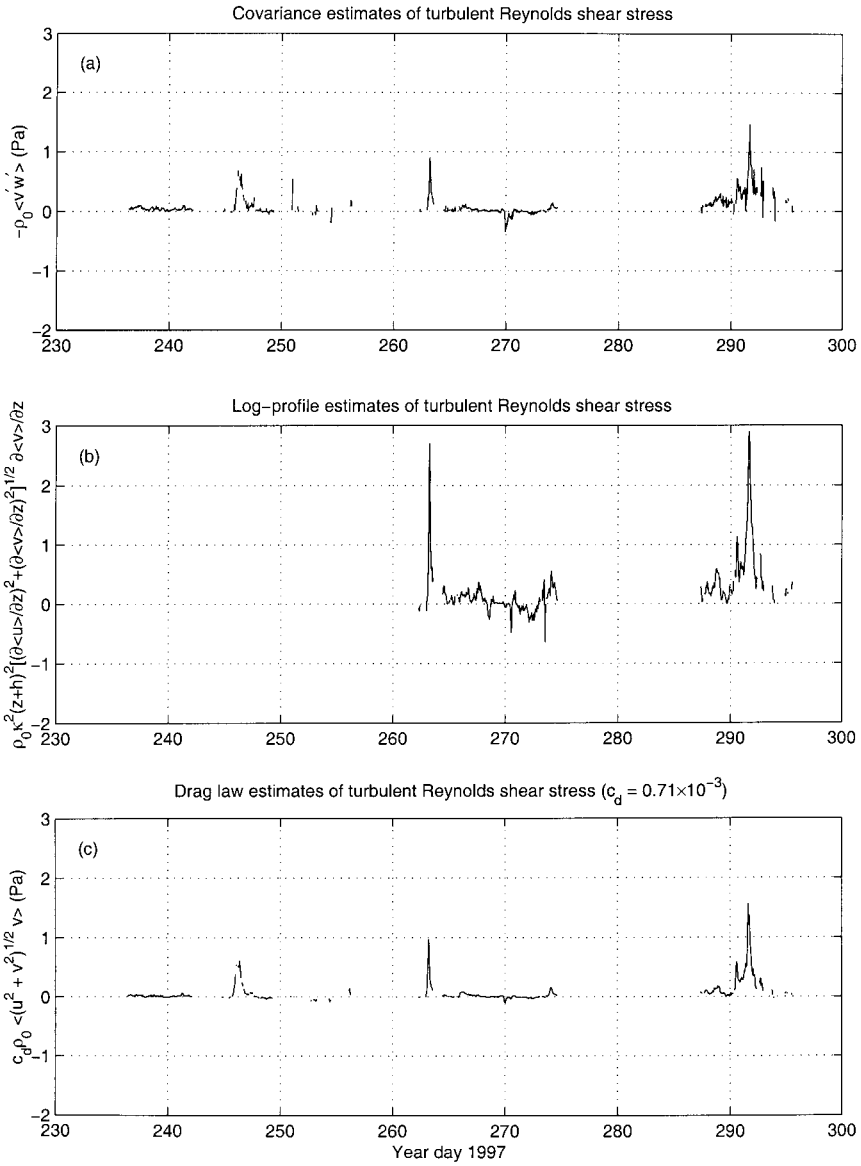

FIG. 9. (a) Covariance, (b) log profile, and (c) drag law estimates of turbulent Reynolds shear stress vs time.

tributed negligibly to shoreward fluxes of alongshore momentum at the ADV frame, indicating that shear waves had a small effect on the alongshore momentum balance. The pressure term neglected in (1) is $O(\rho_0 gh\partial\overline{\eta}/\partial y)$, where g is gravitational acceleration. To produce dynamically significant values of $O(1$ Pa) at $h = 4.5$ m, the alongshore surface slope $\partial\overline{\eta}/\partial y$ must be $O(2 \times 10^{-5})$. Measurements sufficient to resolve slopes of this magnitude were not obtained. Previous pressure measurements at the same site at alongshore separations of tens of kilometers (Lentz et al. 1999) indicate that peak alongshore surface slopes were an order of magnitude smaller than 2×10^{-5} (S. Lentz 2000, personal communication), but larger gradients might have occurred at smaller scales, for example, because of alongshore variability in wave statistics produced by alongshore-nonuniform bathymetry. A typical advective term neglected in (1) is $O(\rho_0 h\overline{v}\partial\overline{v}/\partial y)$. To produce dynamically significant values of $O(1$ Pa) at $h = 4.5$ m during strong flows with $\overline{v} = O(1)$ m s^{-1}, $\partial\overline{v}/\partial y$ must be $O(2 \times 10^{-4})$ s^{-1}, corresponding to differences $\Delta\overline{v}$ of $O(0.04)$ m s^{-1} at an alongshore separation of 200 m. Velocity measurements from electromagnetic sensors 100 m north and south of the ADV frame indicate $\Delta\overline{v}$ exceeding this value, so that advective acceleration possibly is significant. A quantitative assessment, difficult because of measurement uncertainties, is beyond the scope of this study.

b. Energetics, velocity profile, and drag laws

Figure 8 indicates that a balance between shear production and dissipation controlled the energetics of near-bottom turbulence at the ADV frame and that breaking-induced dissipation associated with the shoreward decrease of wave-induced energy flux did not penetrate to the depth of the ADVs. These observations are similar to results in wall-bounded turbulent shear flows in which shear production balances dissipation near the wall (e.g., Tennekes and Lumley 1972). The observations are inconsistent with the simplest model of surf zone turbulence (Battjes 1975), in which breaking-induced dissipation is assumed to be distributed uniformly over the water depth, and they also are inconsistent with empirical results for locally forced waves in deep water (e.g., Terray et al. 1996), which indicate penetration of breaking-induced turbulence to depths of a few times the significant wave height, which exceeds the water depth in the surf zone. However, the observations are qualitatively consistent with Svendsen's (1987) analysis of laboratory measurements, which indicates that only a small fraction (2%–5%) of the dissipation associated with breaking waves in the surf zone occurs below trough level.

Possible explanations of the factor of 2 differences between the left and right sides of (3) (Fig. 9), indicating departure from the Prandtl–von Kármán velocity profile, include inaccurate estimates of $-\rho_0\overline{v'w'}$, discussed in section 4a, and stable stratification owing to temperature, salinity, or suspended sediment (e.g., Monin and Yaglom 1971). When combined with ADP estimates of velocity gradient, estimates of buoyancy frequency N obtained from daily measurements of conductivity, temperature, and depth (CTD) at the end of the pier (Fig. 2) yield gradient Richardson numbers $\mathrm{Ri} = N^2/(\partial\overline{v}/\partial z)^2$ less than roughly 0.01 during the strong events that dominate in Fig. 9, indicating a negligible effect on the structure of the time-averaged velocity profile (e.g., Businger et al. 1971). A commonly used model of stratification by suspended sediment (e.g., Glenn and Grant 1987) is

$$\frac{\kappa(z + h)}{u_*}\left|\frac{\partial\overline{v}}{\partial z}\right| = 1 + \beta\frac{z + h}{L}, \qquad (11)$$

where $u_* = |\overline{v'w'}|^{1/2}$ is shear velocity, β is an empirical constant approximately equal to 5 (Hogstrom 1988), and L is the Monin–Obukhov length, defined for stratification by sediments in steady state by

$$L = \frac{u_*^3}{\kappa g(s - 1)w_s\overline{c}}, \qquad (12)$$

where s and w_s are specific gravity and settling velocity of the sediments, respectively, and $\overline{c}$ is time-averaged sediment concentration by volume. With $s = 2.65$ and $w_s = 0.02$ m s^{-1}, typical of beach sands at Duck (Stauble 1992), (11) and (12) imply that $\overline{c}$ must be $O(4 \times 10^{-5})$ at the ADVO measurement height $z + h \simeq 0.85$ m to balance the left and right sides of (3) during strong events. Concentration measurements sufficient to test this computation were not obtained at the ADV frame. A model of the vertical distribution of suspended sediment in turbulent shear flows [Eq. (15) of Taylor and Dyer 1977] suggests that concentrations of this magnitude are unlikely because rapid decay of $\overline{c}$ with z requires $\overline{c} = O(1)$ (pure sediment and no water) at $z \simeq 0.2$ m, which clearly is implausible, to produce $\overline{c} = O(4 \times 10^{-5})$ at $z + h = 0.85$ m. However, this calculation is sensitive to the poorly constrained turbulent Prandtl number for sediments, and the model of sediment distribution has not been tested in the surf zone.

The drag coefficient estimated from (4) for unbroken waves [$c_d = (1.9 \pm 0.2) \times 10^{-3}$] is consistent with a previous nearshore estimate seaward of the surf zone (Feddersen et al. 1998). However, the smaller drag coefficient determined for breaking waves [$c_d = (0.71 \pm 0.03) \times 10^{-3}$] is smaller than other estimates obtained in the surf zone (Thornton and Guza 1986; Whitford and Thornton 1996) and contradicts studies that produced larger estimates of drag coefficients under breaking waves than under nonbreaking waves (Feddersen et al. 1998; Lentz et al. 1999). A reduced c_d under breaking waves is plausible because large wave-induced velocities destroyed bedforms (Hanes and Alymov 2000, submitted to *J. Geophys. Res.*), and breaking-induced turbulence did not penetrate to the measurement depth (Fig. 8). In addition, stable stratification by suspended sediments may have occurred near the seafloor, increasing $\partial\overline{v}/\partial z$ and thus $\overline{v}$ for a fixed bottom stress (e.g., Taylor and Dyer 1977). Alternatively, the small c_d observed here under breaking waves could result from inaccurate estimates of $\rho_0\overline{v'w'}$ (section 4a). If the true $\rho_0\overline{v'w'}$ under breaking waves is twice as large as indicated by estimates based on (5), c_d would double and the momentum balance (1) would close. However, a doubling of $-\rho_0\overline{v'w'}$ would cause a factor of 2 more shear production (Fig. 8a) than dissipation (Fig. 8b).

5. Summary and conclusions

Measurements of turbulence, waves, currents, and wind permit examination of 1) an approximate alongshore momentum balance between wind stress, cross-shore gradient of wave-induced radiation stress, and near-bottom turbulent Reynolds stress; 2) an approximate turbulence energy balance, in which dissipation balances the sum of shear production and the depth-averaged rate at which breaking extracts energy from the shoaling wave field; 3) the Prandtl–von Kármán representation of the velocity profile in a wall-bounded shear flow; and 4) a quadratic drag law. The results are dominated by three events when large winds and waves forced strong flows, and the sensors were in the outer part of the surf zone. Estimates of near-bottom turbulent Reynolds shear stress are smaller than the sum of wind and wave forcing by a factor of approximately 2. In the turbulent energy balance shear production balances dis-

sipation, and both are two orders of magnitude smaller than the depth-averaged rate of energy loss by the shoaling wave field, suggesting that breaking-induced turbulence did not extend to the measurement depth. Near-bottom velocity gradients are larger by approximately 50% than indicated by the Prandtl–von Kármán logarithmic velocity law, given estimates of bottom stress. The bottom drag coefficient for unbroken waves is similar to a previous nearshore estimate outside of the surf zone, but the drag coefficient for breaking waves is smaller than values from previous results based on indirect estimates of bottom stress.

The reasons for the imbalances in the momentum equation and the Prandtl–von Kármán velocity profile are not known. However, turbulent Reynolds shear stress was central to these balances, and the technique for estimation of stress is based on the explicit assumption that the spatial scales of the stress-carrying near-bottom motions are smaller than the height above bottom. The present measurements are not sufficient to test this assumption. Determining the spatial scales of the stress-carrying motions in wave-driven nearshore flows is an important question for future research. Other unresolved questions include the adequacy of linear theory to estimate the cross-shore gradient of wave-induced radiation stress in breaking waves, the role of nonlinear advective terms and pressure gradient in the alongshore momentum balance, the effect of bedforms and suspended sediments on nearshore flows, and the vertical structure of dissipation in the surf zone.

Acknowledgments. Staff from the Field Research Facility, Duck, NC, and the Center for Coastal Studies, Scripps Institution of Oceanography, deployed, maintained, and recovered the instruments in harsh surf zone conditions. R. T. Guza, T. H. C. Herbers, B. Raubenheimer, and W. C. O'Reilly helped design and manage the field experiment and provided high-quality processed measurements of wave statistics and currents. P. Howd planned, obtained, and processed the ADP measurements. J. Fredericks, G. Voulgaris, and A. Williams obtained the ADV measurements, and J. Fredericks processed the ADV data. J. Edson obtained and processed the wind measurements. S. Lentz and F. Feddersen provided useful comments on the manuscript. Funding was provided by the Office of Naval Research, the National Science Foundation, the Mellon Foundation, and the Woods Hole Oceanographic Institution's Rinehart Coastal Research Center.

APPENDIX

Model of High-Frequency Turbulent Velocity Spectra

The purpose of the appendix is to derive the models (6) and (7) for the high-frequency spectra of near-bottom velocities measured by a point sensor past which inertial-range turbulence is advected by a mean current and wave-induced velocities. It is convenient to use indicial notation, in which the coordinates are (x_1, x_2, x_3), where x_3 is vertical, and the corresponding turbulent velocity vector is (u_1', u_2', u_3'). The starting point is Eq. (A11) of Lumley and Terray (1983):

$$P_{ij}(\omega) = \frac{1}{2\pi}\int_{-\infty}^{+\infty} d\tau\, \exp(-i\omega\tau) \int_{\mathbf{k}} \phi_{ij}(\mathbf{k})\, \exp(i\mathbf{k}\cdot\mathbf{U}\tau)\, \exp\left[-\frac{1}{2}(k_1^2\sigma_1^2 + k_2^2\sigma_2^2 + k_3^2\sigma_3^2)\tau^2\right] d^3\mathbf{k}. \quad \text{(A1)}$$

Here ω is radian frequency, P_{ij} is the measured turbulence spectrum, defined so that $\int_{-\infty}^{+\infty} P_{ij}(\omega)\, d\omega = \overline{u_i' u_j'}$, τ is a dummy variable of integration, ϕ_{ij} is the spectrum tensor of the turbulence (e.g., Batchelor 1967), $\mathbf{k}$ is the wavenumber vector, $\mathbf{U}$ is the mean velocity vector, and σ_1^2, σ_2^2, and σ_3^2 are the nonzero elements of the covariance tensor of the wave-induced velocity vector, which has been diagonalized. Equation (A1) is an asymptotic result for frequencies large in comparison with the dominant wave frequency. Of particular interest are $P_{11}(\omega) + P_{22}(\omega)$ and $P_{33}(\omega)$, which are invariant under coordinate rotations about the x_3 axis.

Several idealizations simplify the analysis. The turbulence is assumed to be homogeneous and isotropic:

$$\phi_{ij} = \frac{E(k)}{4\pi k^2}\left(\delta_{ij} - \frac{k_i k_j}{k^2}\right), \quad \text{(A2)}$$

and to have a Kolmogorov spectrum:

$$E(k) = \alpha\epsilon^{2/3}k^{-5/3} \quad \text{(A3)}$$

(e.g., Batchelor 1967). Here $E(k)$ is the isotropic energy spectrum, k is the magnitude of $\mathbf{k}$, δ_{ij} is the Kronecker delta, α is the empirical Kolmogorov constant, and ϵ is the dissipation rate. In addition, attention is restricted to cases with $\sigma_3 = 0$ and $U_3 = 0$, which is appropriate for near-bottom applications, and to cases with waves that are narrowbanded in direction so that $\sigma_2 = 0$, where, without loss of generality, x_1 is defined to be the direction of wave propagation. Substitution of (A2) and (A3) into (A1), and use of standard results to evaluate the τ integral (e.g., Gradshteyn and Ryzhik 1965), yields

$$P_{ij} = \frac{\alpha\epsilon^{2/3}}{2(2\pi)^{3/2}} \int_{\mathbf{k}} \frac{d^3\mathbf{k}}{k^{11/3}(k_1^2\sigma_1^2)^{1/2}}\left(\delta_{ij} - \frac{k_i k_j}{k^2}\right)$$

$$\times \exp\left\{-\frac{[k_1 V\cos(\theta) + k_2 V\sin(\theta) - \omega]^2}{2k_1^2\sigma_1^2}\right\}, \quad \text{(A4)}$$

where $V\cos(\theta) = U_1$ and $V\sin(\theta) = U_2$, with $V \geq 0$.

For the special case $i = j = 3$, the k_3 integral in (A4) can be evaluated in terms of gamma functions (e.g., Abramowitz and Stegun 1972), leading to

$$P_{33} = \frac{2\sqrt{2}}{55\pi}\frac{\Gamma(1/3)}{\Gamma(5/6)}\alpha\epsilon^{2/3} \times \int_{-\infty}^{+\infty}\int_{-\infty}^{+\infty}\frac{dk_1 dk_2}{(k_1^2 + k_2^2)^{4/3}(k_1^2\sigma_1^2)^{1/2}} \times \exp\left\{-\frac{[k_1 V\cos(\theta) + k_2 V\sin(\theta) - \omega]^2}{2k_1^2\sigma_1^2}\right\}. \quad \text{(A5)}$$

For the contraction P_{ii}, the k_3 integral similarly can be evaluated in terms of gamma functions, and it follows that

$$P_{11}(\omega) + P_{22}(\omega) = \frac{7}{4}P_{33}(\omega) \quad \text{(A6)}$$

so that, once P_{33} has been determined, $P_{11} + P_{22}$ is also known. Therefore attention is restricted to P_{33}.

Two sets of transformations of (A5) are necessary. The first is substitution of $y = k_2/k_1$, with special attention to the behavior near $k_1 = 0$ and near $k_1 \to \pm\infty$, followed by substitution of $x = \omega/(k_1 V)$, which leads to

$$P_{33} = \frac{2\sqrt{2}}{55\pi}\frac{\Gamma(1/3)}{\Gamma(5/6)}\frac{\alpha\epsilon^{2/3}V^{5/3}}{\sigma_1\omega^{5/3}}\int_{-\infty}^{+\infty}\int_{-\infty}^{+\infty}\exp\left\{-\frac{V^2[\cos(\theta) + y\sin(\theta) - x]^2}{2\sigma_1^2}\right\}\frac{(x^2)^{1/3}\,dx\,dy}{(1 + y^2)^{4/3}}. \quad \text{(A7)}$$

The second is substitution in (A7) of $y' = y - x/\sin(\theta)$, followed by substitution of $x' = x/\sin(\theta)$, which yields

$$P_{33} = \frac{2\sqrt{2}}{55\pi}\frac{\Gamma(1/3)}{\Gamma(5/6)}\frac{\alpha\epsilon^{2/3}V^{5/3}\sin^{5/3}(\theta)}{\sigma_1\omega^{5/3}}\int_{-\infty}^{+\infty}\int_{-\infty}^{+\infty}\exp\left\{-\frac{V^2[\cos(\theta) + y\sin(\theta)]^2}{2\sigma_1^2}\right\}\frac{(x^2)^{1/3}\,dx\,dy}{[1 + (x + y)^2]^{4/3}}, \quad \text{(A8)}$$

where primes have been omitted.

Equation (A8) can be reduced to a single integral by considering two methods of obtaining the pure current limit, $\sigma_1 \to 0$. In this limit, P_{33} does not depend on θ, so θ can be set to zero in (A7). The y integral in (A7) then can be evaluated in terms of gamma functions. In the x integral, the exponential function behaves like a Dirac delta function centered at $x = 1$ in the limit $\sigma_1 \to 0$, so x can be set to unity except in the exponential, which permits straightforward evaluation. The result of these operations is

$$\lim_{\sigma_1\to 0} P_{33} = \frac{12}{55}\alpha\epsilon^{2/3}V^{2/3}\omega^{-5/3}, \quad \text{(A9)}$$

which is consistent with results for steady flows (Batchelor 1967). Alternatively, as $\sigma_1 \to 0$ in (A8), the exponential acts like a delta function centered at $y = -\cot(\theta)$ so that y can be replaced by $-\cot(\theta)$ in all terms except the exponential. The y integral can then be evaluated, yielding

$$\lim_{\sigma_1\to 0} P_{33} = \frac{4}{55\sqrt{\pi}}\frac{\Gamma(1/3)}{\Gamma(5/6)}\frac{\alpha\epsilon^{2/3}V^{2/3}\sin^{2/3}(\theta)}{\omega^{5/3}} \times \int_{-\infty}^{+\infty}\frac{(x^2)^{1/3}\,dx}{\{1 + [x - \cot(\theta)]^2\}^{4/3}}. \quad \text{(A10)}$$

Equations (A9) and (A10) must be equal, so that

$$\int_{-\infty}^{+\infty}\frac{(x^2)^{1/3}\,dx}{\{1 + [x - \cot(\theta)]^2\}^{4/3}} = \frac{3\sqrt{\pi}\Gamma(5/6)}{\Gamma(1/3)\sin^{2/3}(\theta)}. \quad \text{(A11)}$$

Substitution of $y = \cot(\theta)$ gives

$$\int_{-\infty}^{+\infty}\frac{(x^2)^{1/3}\,dx}{[1 + (x + y)^2]^{4/3}} = 3\sqrt{\pi}\frac{\Gamma(5/6)}{\Gamma(1/3)}(1 + y^2)^{1/3}, \quad \text{(A12)}$$

which is an evaluation of the x integral in (A8). Substitution of (A12) into (A8) and use of a change of variables leads to (7), where

$$I\left(\frac{\sigma}{V},\,\theta\right) = \frac{1}{\sqrt{2\pi}}\left(\frac{\sigma}{V}\right)^{2/3}\int_{-\infty}^{+\infty}\left[x^2 - 2\frac{V}{\sigma}\cos(\theta)x + \frac{V^2}{\sigma^2}\right]^{1/3}\exp\left(-\frac{1}{2}x^2\right)dx, \quad \text{(A13)}$$

an integral that easily is evaluated numerically. Use of (A6) then gives (6).

REFERENCES

Abramowitz, M., and I. A. Stegun, 1972: *Handbook of Mathematical Functions.* Natl. Bur. of Stand., 1046 pp.

Batchelor, G. K., 1967: *The Theory of Homogeneous Turbulence.* Cambridge University Press, 197 pp.

Battjes, J. A., 1975: Modeling of turbulence in the surf zone. *Symp. on Modelling Techniques, MODELING75,* Vol. 2, San Francisco, CA, American Society of Civil Engineers, 1050–1061.

——, 1988: Surf-zone dynamics. *Annu. Rev. Fluid Mech.,* **20,** 257–293.

Birkemeier, W. A., H. C. Miller, S. D. Wilhelm, A. D. DeWall, and C. S. Gorbics, 1985: A user's guide to the Coastal Engineering Research Center's (CERC's) Field Research Facility. Instr. Report CERC-85-1, U.S. Army Corps of Engineers Waterways Experiment Station, Coastal Engineering Research Center, Vicksburg, MS, 136 pp.

Bowen, A. J., 1969: The generation of longshore currents on a plane beach. *J. Mar. Res.,* **27,** 206–215.

——, and R. A. Holman, 1989: Shear instabilities of the mean longshore current. 1. Theory. *J. Geophys. Res.,* **94,** 18 023–18 030.

Businger, J. A., J. C. Wyngaard, Y. Izumi, and E. F. Bradley, 1971: Flux–profile relationships in the atmospheric surface layer. *J. Atmos. Sci.,* **28,** 181–189.

Elgar, S., T. H. C. Herbers, and R. T. Guza, 1994: Reflection of ocean surface gravity waves from a natural beach. *J. Phys. Oceanogr.,* **24,** 1503–1511.

——, R. T. Guza, T. H. C. Raubenheimer, and E. Gallagher, 1997: Spectral evolution of shoaling and breaking waves on a barred beach. *J. Geophys. Res.,* **102,** 15 797–15 805.

——, B. Raubenheimer, and R. T. Guza, 2001: Current meter performance in the surf zone. *J. Atmos. Oceanic Technol.,* in press.

Feddersen, F., R. T. Guza, S. Elgar, and T. H. C. Herbers, 1998: Alongshore momentum balances in the nearshore. *J. Geophys. Res.,* **103,** 15 667–15 676.

Fredericks, J. J., J. H. Trowbridge, and G. Voulgaris, 2001: Turbulence in the shallow nearshore environment during SandyDuck 97. Woods Hole Oceanographic Institution, Tech. Rep., WHOI-2001-02, Woods Hole, MA, 45 pp.

Fredsoe, J., and R. Deigaard, 1992: *Mechanics of Coastal Sediment Transport.* World Scientific, 369 pp.

Garcez Faria, A. F., E. B. Thornton, T. P. Stanton, C. V. Soares, and T. C. Lippmann, 1998: Vertical profiles of longshore currents and related bed shear stress and bottom roughness. *J. Geophys. Res.,* **103** (C2), 3217–3232.

George, R., R. E. Flick, and R. T. Guza, 1994: Observations of turbulence in the surf zone. *J. Geophys. Res.,* **99,** 801–810.

Glenn, S. M., and W. D. Grant, 1987: A suspended sediment stratification for combined wave and current flows. *J. Geophys. Res.,* **92,** 8244–8264.

Gradshteyn, I. S., and I. M. Ryzhik, 1965: *Table of Integrals, Series, and Products.* Academic Press, 1160 pp.

Grant, H. L., R. W. Stewart, and A. Moilliet, 1962: Turbulence spectra from a tidal channel. *J. Fluid Mech.,* **12,** 241–263.

Herbers, T. H. C., S. Elgar, and R. T. Guza, 1995: Generation and propagation of infragravity waves. *J. Geophys. Res.,* **100,** 24 863–24 872.

——, ——, and ——, 1999: Directional spreading of waves in the nearshore. *J. Geophys. Res.,* **104,** 7683–7693.

——, N. R. Russnogle, and S. Elgar, 2000: Spectral energy balance of breaking waves within the surf zone. *J. Phys. Oceanogr.,* **30,** 2723–2737.

Hogstrom, U., 1988: Non-dimensional wind and temperature profiles in the atmospheric surface layer: A re-evaluation. *Bound.-Layer Meteor.,* **42,** 55–78.

Jeffreys, H., 1974: *Cartesian Tensors.* Cambridge University Press, 92 pp.

Kaihatu, J., and J. Kirby, 1995: Nonlinear transformation of waves in finite water depth. *Phys. Fluids,* **7,** 1903–1914.

Kaimal, J. C., J. C. Wyngaard, and D. A. Haugen, 1968: Deriving power spectra from a three-component sonic anemometer. *J. Appl. Meteor.,* **7,** 827–837.

Lentz, S., R. T. Guza, S. Elgar, F. Feddersen, and T. H. C. Herbers, 1999: Momentum balances on the North Carolina inner shelf. *J. Geophys. Res.,* **104,** 18 205–18 226.

Longuet-Higgins, M. S., 1970: Longshore currents generated by obliquely incident sea waves. Part 1 and 2. *J. Geophys. Res.,* **75,** 6790–6801.

Lumley, J. L., and E. A. Terray, 1983: Kinematics of turbulence convected by a random wave field. *J. Phys. Oceanogr.,* **13,** 2000–2007.

Mei, C. C., 1983: *The Applied Dynamics of Ocean Surface Waves.* McGraw-Hill, 740 pp.

Monin, A. S., and A. M. Yaglom, 1971: *Statistical Fluid Mechanics.* The MIT Press, 769 pp.

Nielsen, P., 1992: *Coastal Bottom Boundary Layers and Sediment Transport.* World Scientific, 257 pp.

Ogston, A. S., C. R. Sherwood, and A. E. Asher, 1995: Estimation of turbulence dissipation rates and gas-transfer velocities in a surf pool: Analysis of the results from WABEX-93. *Air–Water Gas Transfer: Selected Papers from the Third International Symposium on Air–Water Gas Transfer, Heidelberg University,* B. Jahne and E. C. Monahan, Eds., AEON Verlag, 255–268.

Oltman-Shay, J., P. A. Howd, and W. A. Birkemeier, 1989: Shear instabilities of the mean long-shore current. Part 2. Field data. *J. Geophys. Res.,* **94,** 18 031–18 042.

Stauble, D. K., 1992: Long-term profile and sediment morphodynamcis: Field Research Facility case history. Tech. Rep. CERC-92-7, U. S. Army Corps of Engineers Waterways Experiment Station, Coastal Engineering Research Center, Vicksburg, MS, 252 pp.

Svendsen, I. A., 1987: Analysis of surf zone turbulence. *J. Geophys. Res.,* **92,** 5115–5124.

——, and U. Putrevu, 1994: Nearshore mixing and dispersion. *Proc. Roy. Soc. London,* **445A,** 561–576.

Taylor, P. A., and K. A. Dyer, 1977: Theoretical models of flow near the bed and their implications for sediment transport. *The Sea.* Vol. 6: *Marine Modeling,* E. D. Goldberg, I. N. McCave, J. J. O'Brien, and J. H. Steele, Eds., Wiley and Sons, 579–601.

Tennekes, H., and J. L. Lumley, 1972: *A First Course in Turbulence.* The MIT Press, 300 pp.

Terray, E. A., M. A. Donelan, Y. C. Agrawal, W. M. Drennan, K. K. Kahma, A. J. Williams, P. A. Hwang, and S. A. Kitaigorodskii, 1996: Estimates of kinetic energy dissipation under breaking waves. *J. Phys. Oceanogr.,* **26,** 792–807.

Thornton, E. B., and R. T. Guza, 1986: Surf-zone longshore currents and random waves: Field data and models. *J. Phys. Oceanogr.,* **16,** 1165–1178.

Ting, F. C. K., and J. T. Kirby, 1996: Dynamics of surf-zone turbulence in a spilling breaker. *Coastal Eng.,* **27,** 131–160.

Trowbridge, J. H., 1998: On a technique for measurement of turbulent shear stress in the presence of surface waves. *J. Atmos. Oceanic Technol.,* **15,** 290–298.

Voulgaris, G., and J. H. Trowbridge, 1998: Evaluation of the acoustic Doppler velocimeter (ADV) for turbulence measurements. *J. Atmos. Oceanic Technol.,* **15,** 272–289.

Whitford, D. J., and E. B. Thornton, 1996: Bed shear stress coefficients for longshore currents over a barred profile. *Coastal Eng.,* **27,** 243–262.